Biomass Conversion and Biorefinery (2022) 12:2185–2202
https://doi.org/10.1007/s13399-020-00739-5

ORIGINAL ARTICLE

Facile preparation of magnetic porous carbon monolith from waste corrugated cardboard box for solar steam generation and adsorption

Yuhui Ma[1] · Junrui Cao[1,2]

Received: 17 February 2020 / Revised: 7 April 2020 / Accepted: 23 April 2020 / Published online: 8 May 2020

Abstract

Porous carbon monoliths (PCMs) were prepared from waste corrugated cardboard box (WCCB) via slurrying in $FeCl_3$ solution followed by molding and thermal treatment. The thermal process was analyzed by a thermogravimetric analyzer coupled with a Fourier transform infrared spectrometer. The evolution of physicochemical characteristics of PCMs was studied. The photothermal conversion and solar steam generation performances of the optimal sample ($PCM_{Fe/600}$) were evaluated. The adsorption properties of $PCM_{Fe/600}$ for methylene blue (MB) were investigated. Results showed that Fe^{3+} promoted the breaking of cellulose chains in WCCB, leading to the occurrence of pyrolysis of WCCB at lower temperatures and the reduction of activation energy by 76.63 kJ mol^{-1}. Char yield raised because volatile radicals were captured by $FeCl_3$-derived amorphous Fe(III) species, then involved in char formation. Amorphous Fe(III) continuously converted into Fe_3O_4 crystallites with carbonization temperature increasing from 400 to 700 °C, then α-Fe was formed at 800 °C via the carbothermal reduction of Fe_3O_4. $FeCl_3$ was favorable to the formation of a developed microporous structure. Surface area significantly increased with carbonization temperature increasing from 400 to 600 °C due to the removal of volatiles. The etching of carbon by Fe_3O_4 above 700 °C also led to the increase of surface area. $PCM_{Fe/600}$ exhibited higher optical absorption than other samples due to its high graphite degree and porosity. It also had excellent photothermal performance; thus, solar steam yield was 1.46 times that of the pure water with the assistance of $PCM_{Fe/600}$. $PCM_{Fe/600}$ in floating state was effective in adsorption of MB from water. Besides, the adsorption behavior fitted Langmuir model with a monolayer adsorption capacity reached up to 70.9 mg g^{-1}.

Keywords Waste corrugated cardboard box · Magnetic porous carbon monolith · TG-FTIR · Solar steam generation · Adsorption

1 Introduction

Solar steam generation (SSG) has a great application prospect in producing clean drinkable water from polluted water at zero CO_2 emission, since it uses the renewable and abundant solar energy as the only energy source [1, 2]. In typical SSG systems, solar energy is harvested and converted to thermal energy by photothermal materials and the thermal energy is used to heat up liquid water to generate steam [3]. Many efforts have been devoted to developing advanced photothermal materials, which have made the old concept of SSG become a rejuvenated green technology [4]. Carbonaceous materials are inherently suitable for broad light absorption owing to the π-band's optical transitions. Their optically excited electrons can quickly relax via thermalization due to electron-electron and electron-phonon scattering [5]. Various carbonaceous materials, such as graphene, graphene oxide (GO), carbon nanotube (CNT), graphite, carbon black, etc. have been investigated as the photothermal materials [6]. Although CNT and graphene are two representative kinds of carbonaceous materials for SSG, both of them are still more expensive than gold. Moreover, the fabrication of graphene or CNT-based photothermal materials is complicated, making them unrealistic for widespread use [7, 8]. Therefore, it is highly desirable to develop inexpensive, easy-to-manufacture, mechanically robust carbonaceous materials for SSG [9].

Adsorption is considered as another effective technology for water purification due to its convenience for operation, effectiveness, and low consumption [10]. Carbonaceous

✉ Yuhui Ma
myhbiomass@163.com

[1] The Institute of Seawater Desalination and Multipurpose Utilization, Ministry of Natural Resources of the People's Republic of China, Tianjin 300192, China

[2] Tianjin Haiyue Water Treatment High-tech Co., Ltd., Tianjin 300192, China

materials with developed porous structure are commonly used as adsorbents by adsorbing pollutants from water. Porous carbon materials have been applied in the removal of nutrients [11], heavy metals [12], antibiotics [13], dyes [14], and natural organic matter [15]. Recently, the "treating contaminants with wastes" strategy has been considered as an inspiring approach to reducing the costs of contaminated water purification, and it has triggered the studies focused on the production of porous carbon materials from organic wastes, such as crab shell [16, 17], garlic skin [13], oil palm sell [18], rice husk [19], waste tire [20], and so on.

With the fast development of E-commerce in China, the express industry is undergoing unprecedented growth. The more people choose to shop online, the more delivery packages are need. In China, the number of corrugated cardboard box used for express packages increased from 9.92 billion in 2015 to 14.4 billion in 2016. Waste corrugated cardboard boxes (WCCB) have became one of the main constituents of municipal solid waste (MSW) in China, but less than 20% of them are collected and reused [21, 22]. Therefore, it is of great environmental and economic significance to develop a facile and feasible way for the recycling of WCCB. Since WCCB consists mainly of cellulose fibers [23, 24], it is an interesting subject to utilize WCCB as a carbonaceous precursor for porous carbon materials, which can simultaneously be used for SSG and adsorption.

Herein, we proposed a facile way of preparing a low-cost multi-functional porous carbon monolith (PCM) using WCCB as the raw material. The PCM can be used for SSG and adsorption because of its good photothermal conversion and absorption properties. The evolution of the physicochemical characteristics of the samples was analyzed by X-ray diffraction (XRD), N_2-adsorption/desorption, Raman spectroscopy, ultraviolet visible near infrared spectroscopy (UV-Vis-NIR), and scanning electron microscope (SEM). Pyrolysis kinetic and preparation mechanism were revealed by a thermogravimetric analyzer coupled with Fourier transform infrared spectrometer (TG-FTIR).

2 Experimental

2.1 Materials

WCCB was collected from local offices and cut into small square-shaped pieces (about 1 cm × 1 cm in size) and then stored in polyethylene bags until needed. $FeCl_3{\cdot}6H_2O$ of analytical grade was purchased from Sinopharm, China. Methylene blue (MB) (chemical formula: $C_{16}H_{18}ClN_3S_3{\cdot}H_2O$) was purchased from Tianjin Fuchen chemical reagents factory.

2.2 Preparation of porous carbon monolith

$FeCl_3$ solution (2 wt%) was prepared by dissolving $FeCl_3{\cdot}6H_2O$ in deionized water, and WCCB pieces were dipped into $FeCl_3$ solution using a weight ratio: $FeCl_3$/WCCB of 1/1 (on a dry basis). The mixture was vigorously stirred at room temperature for 24 h, then the uniform slurry was poured into tea filter bags for pre-dehydration. The pre-dehydrated material was placed in a manual tapping mold for further dehydration and molding into tablets, then the tablets were dried in an oven at 80 °C for 24 h. The dry tablets (labeled as Fe-WCCB) with diameter of 1.79 cm, and thickness of 0.61 cm were heated at a temperature increasing by 5 °C min^{-1} to final carbonization temperatures of 300, 400, 500, 600, 700, and 800 °C under pure N_2 atmosphere with the flow rate of 200 mL min^{-1} in a tube furnace (CTF12/65/550, Carbolite, Great Britain), and the final temperature was maintained for 2 h. The carbonized products were cooled in pure N_2 flow, and denoted $PCM_{Fe/300}$, $PCM_{Fe/400}$, $PCM_{Fe/500}$, $PCM_{Fe/600}$, $PCM_{Fe/700}$, and $PCM_{Fe/800}$, respectively, where PCM represents "porous carbon monolith." For comparison, the tablets (labeled as H_2O-WCCB) were obtained from WCCB according to the same process except using deionized water rather than $FeCl_3$ for slurrying. The carbonized product (labeled as PCM_{800}) was prepared from H_2O-WCCB at 800 °C under the same heating and atmospheric conditions. The yield of product was calculated from the following equation:

$$Yield(\%) = \frac{M_{PCM}}{M_{Pre}} \times 100 \quad (1)$$

where M_{PCM} is the mass of the porous carbon monolith, and M_{Pre} is the mass of Fe-WCCB or H_2O-WCCB used as carbon precursor. The fabrication process of the porous carbon monolith is illustrated in Fig. 1.

2.3 Characterization of porous carbon monolith

X-ray diffraction (XRD) analysis was carried out using an X-ray diffractometer (Bruker D8, Germany). N_2-adsorption/desorption analysis was performed using a gas adsorption apparatus (Autosorb-iQ, Quantachrome Instruments, USA) at − 196 °C. BET surface area (S_{BET}) was calculated using Brunauer-Emmett-Teller (BET) method. Total pore volume (V_{Total}) was estimated from liquid volume of N_2 adsorbed at the saturation of relative pressure. Micropore volume (V_{Micro}) and the mesopore volume (V_{Meso}) were deduced using the Horvath-Kawazo (HK) and Barret-Joyner-Halenda (BJH) method, respectively. The average pore diameter (D_{Avg}) was calculated as $D_{Avg} = 4V_{Total}/S_{BET}$. The carbonaceous structures of the

Fig. 1 Fabrication process of porous carbon monolith

samples were acquired by a Raman spectrometer (DXR, Thermo Scientific, USA). Optical absorption spectrum was measured using an ultraviolet-visible-near infrared (UV-Vis-NIR) spectrophotometer (Lambda 950, PerkinElmer, USA). The morphology was observed by using a field emission scanning electron microscope (FE-SEM) (Sigma 500, ZEISS, Germany). All thermal images were taken via an infrared (IR) camera (TiS10, Fluke, USA), and the change of temperature of the samples was also monitored by the IR camera.

2.4 Solar steam generation experiment

Figure 2 shows the experimental setup used to measure the mass loss of water. The optimum sample ($PCM_{Fe/600}$) was embedded in the central circular hole in a slice of expandable polyethylene (EPE) foam, and the assembly structure can float on the surface of water with only the bottom side of $PCM_{Fe/600}$ in direct contact with bulk water. A xenon lamp (HM-Xe330W, Hongming Instrument, China) was used as the solar light source, and the mass change of the water under 0.25 sun

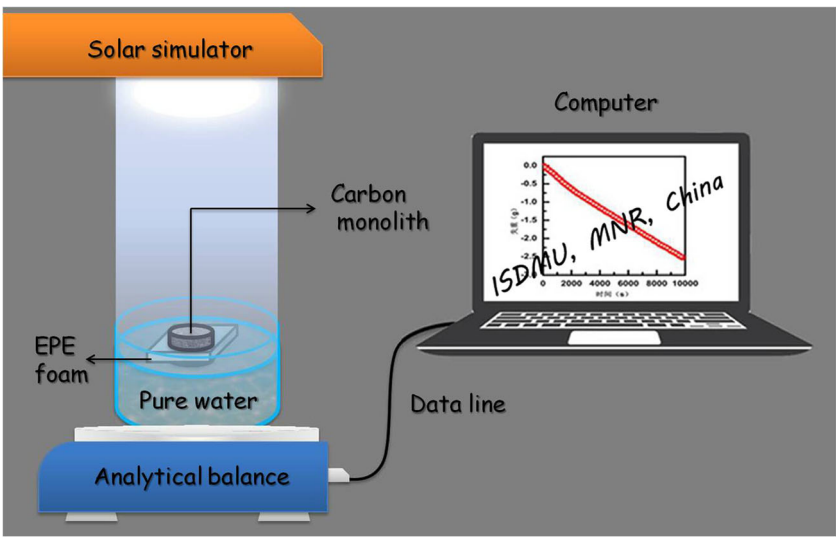

Fig. 2 Experimental setup of solar steam generation test

(250 W m^{-2}) was recorded in real-time by an electronic balance (PL2002, METTLER TOLEDO, Switzerland) and transmitted to a computer.

2.5 Adsorption experiment

Adsorption isotherms of $PCM_{Fe/600}$ for MB were investigated referring a literature method [25]. $PCM_{Fe/600}$ was ground and passed through a 100 mesh sieve. Equilibrium adsorption were conducted in a set of Erlenmeyer flasks containing 0.015 g $PCM_{Fe/600}$ powder and 25 mL MB solutions with various initial concentrations (20 to 70 mg L^{-1}). The flasks were agitated in a shaker at 200 rpm and 30 °C for 48 h to reach the equilibrium. After above treatments, the suspensions were filtered by 0.45 μm membrane filters, then the filtrates were diluted to suitable concentrations. The MB concentrations in the diluted supernatant solutions were determined using an UV-Vis spectrophotometer (DR5000, HACH, USA) at the maximum wavelengths (λ) of 664 nm. MB uptake per unit mass of adsorbent at equilibrium, q_e (mg g^{-1}), was calculated by

$$q_e = \frac{C_0 - C_e}{W} V \tag{2}$$

where C_0 and C_e (mg L^{-1}) are the initial and equilibrium liquid-phase concentrations of MB. V (L) is the volume of the solution and W (g) is the mass of porous carbon used. The equilibrium data were modeled using Langmuir, Freundlich, and Temkin isotherm models and the model equations are shown in Table 1.

To simulate the process of the purification of natural water body using a floating absorbent, $PCM_{Fe/600}$ embedded in EPE foam was added to a beaker containing 20 mL of MB aqueous solution with the concentration of 10 mg L^{-1}. $PCM_{Fe/600}$ can float on the surface of MB solution with the help of EPE foam, and the beaker was sealed using parafilm and left undisturbed at room temperature. The MB solution was sampled using a pipette every 24 h and the concentration of the sample was determined using the UV-Vis spectrophotometer as mentioned above, then the small amount of solution after analysis was put back into the beaker for further adsorption.

2.6 TG-FTIR analysis

Weight loss behaviors and gaseous products obtained during the pyrolysis and carbonization of Fe-WCCB and H_2O-WCCB were studied online using a TG-FTIR instrument that consists of a simultaneous thermal analyzer (STA 2500 Regulus, NETZSCH, Germany) and a Fourier transform infrared spectrometer (TENSOR II, Bruker, Germany). The samples (about 10 mg) were heated from 40 to 1000 °C at N_2 flowing rate of 70 mL min^{-1} and the heating rate of 20 °C min^{-1}. The volatile products were detected online by FTIR, in which IR spectra were recorded at 4000–650 cm^{-1} with a resolution of 4 cm^{-1}. The transfer pipe and the gas cell in the FTIR were both heated at a constant temperature of 200 °C to minimize secondary reactions.

2.7 Pyrolysis kinetic theory

Kinetic study is important for the design of large-scale reactors to achieve practical production. Coats-Redfern method was used in this study to determine the kinetic parameters of Fe-WCCB and H_2O-WCCB [26].

The rate of conversion, dx/dt, is a linear function of a temperature-dependent rate constant, k, and x temperature-independent function of conversion, $f(\alpha)$:

$$\frac{d\alpha}{dt} = kf(\alpha) \tag{3}$$

where x is conversion degree, t is time. α is expressed as

$$\alpha = (m_i - m_t)/(m_i - m_\infty) \tag{4}$$

where m_i is the initial mass of sample, m_t is the mass of the sample at time t, m_∞ is the final mass of the sample in the reaction.

Table 1 Linear and non-linear forms of Langmuir, Freundlich, and Temkin isotherm models

Model	Non-linear form	Linear form	Plot
Langmuir	$q_e = \frac{q_m K_L C_e}{1+K_L C_e}$	$\frac{C_e}{q_e} = \frac{C_e}{q_m} + \frac{1}{K_L q_m}$	$\frac{C_e}{q_e}$ versus C_e
Freundlich	$q_e = K_F C_e^{1/n}$	$logq_e = logK_F + \frac{1}{n} logC_e$	$logq_e$ versus $logC_e$
Temkin	$q_e = B_T In(A_T C_e)$	$q_e = \frac{RT}{b} InA_T + \frac{RT}{b} InC_e$	q_e versus InC_e

q_m (mg g^{-1}) is the maximum monolayer adsorption capacity of the sorbent, K_L (L mg^{-1}) is the Langmuir constants related to the free energy or net enthalpy of adsorption. K_F (mg g^{-1}) (L mg^{-1})$^{1/n}$ is Freundlich adsorption constant, indicating the relative adsorption capacity of the adsorbent, n represents the adsorption intensity, and values of $n > 1$ indicate favorable nature of adsorption. $B_T = RT/b$, with b (J mol^{-1}), A_T (L g^{-1}), R (8.314 J mol^{-1} K^{-1}) and T (K) are the Temkin constant related to heat of sorption, equilibrium binding constant, gas constant, and absolute temperature, respectively

The reaction rate constant, k, has been described by the Arrhenius expression

$$k = A\exp(-E_a/RT) \quad (5)$$

where A is the pre-exponential factor, E_a is the activation energy, R is the gas constant, and T is the absolute temperature.

For a constant heating rate β during gasification, $\beta = dT/dt$, rearranging Eq. (5) and integrating by using Coats-Redfern method is given by

$$\ln\left[g(\alpha)/T^2\right] = \ln[AR/\beta E_a(1-2RT/E_a)] - E_a/RT \quad (6)$$

As the term of $2RT/E_a$ can be neglected because it is much less than 1, Eq. (6) could be simplified as

$$\ln\left[g(\alpha)/T^2\right] = \ln(AR/\beta E_a) - E_a/RT \quad (7)$$

Various reaction models define $g(\alpha)$ in different ways, and if the correct $g(\alpha)$ is used, plotting $\ln[g(\alpha)/T^2]$ versus $1/T$ should result in a straight line. E_a and A can be determined from the slop and the intercept of the line, respectively. The differential form $f(\alpha)$ and the integrated form $g(\alpha)$ for the basic model employed for the kinetic study of solid-state reactions are provided in Table 2 [27].

3 Results and discussion

3.1 TG-FTIR study

3.1.1 Weight loss behavior

TG and derivative thermogravimetry (DTG) curves of H_2O-WCCB and Fe-WCCB can be seen from Fig. 3. For H_2O-WCCB, the weight loss below 140 °C indicated the loss of moisture, and the major weight loss occurred within the temperature of 250–400 °C, with the maximum weight loss peak at 370 °C, indicating the pyrolysis of cellulose. The weight loss rate of H_2O-WCCB became slow above 400 °C because the thermal decomposition of cellulose finished at this temperature. Instead, the carbonization of carbonaceous matters in the residue became the primary reaction, leading to the release of small molecules at a slow rate. The minor weight loss peak at 740 °C was caused by the decomposition of $CaCO_3$ in the residue, which is one of the commonly used mineral fillers during paper-making [23, 27].

The weight loss of Fe-WCCB can be divided into three stages. The maximum weight loss rate of Fe-WCCB was achieved at 295 °C, and it was much lower than that of WCCB. However, Fe-WCCB had obviously higher weight loss rates between 140 and 320 °C, and its main pyrolysis

Table 2 Most frequently used solid-state reaction mechanism functions

Mechanism	Symbol	$f(\alpha)$	$g(\alpha)$
Reaction order			
Zero order	F_0	1	α
First order	F_1	$1-\alpha$	$-\ln(1-\alpha)$
Second order	F_2	$(1-\alpha)^2$	$(1-\alpha)^{-1}-1$
Mampel power			
Power law, $n = 3/2$	$P_{(2/3)}$	$2/3\alpha^{-1/2}$	$\alpha^{3/2}$
Power law, $n = 1/2$	P_2	$2\alpha^{1/2}$	$\alpha^{1/2}$
Power law, $n = 1/3$	P_3	$3\alpha^{2/3}$	$\alpha^{1/3}$
Power law, $n = 1/4$	P_4	$4\alpha^{3/4}$	$\alpha^{1/4}$
Random nucleation and nuclei growth			
Avrami-Erofeev, $n = 1.5$	$A_{1.5}$	$1.5(1-\alpha)[-\ln(1-\alpha)]^{1/3}$	$[-\ln(1-\alpha)]^{2/3}$
Avrami-Erofeev, $n = 2$	A_2	$2(1-\alpha)[-\ln(1-\alpha)]^{1/2}$	$[-\ln(1-\alpha)]^{1/2}$
Avrami-Erofeev, $n = 3$	A_3	$3(1-\alpha)[-\ln(1-\alpha)]^{2/3}$	$[-\ln(1-\alpha)]^{1/3}$
Avrami-Erofeev, $n = 4$	A_4	$3(1-\alpha)[-\ln(1-\alpha)]^{2/3}$	$[-\ln(1-\alpha)]^{1/4}$
Limiting surface reaction between both phases			
Contracting cylinder	R_2	$2(1-\alpha)^{1/2}$	$1-(1-\alpha)^{1/2}$
Contracting sphere	R_3	$3(1-\alpha)^{2/3}$	$1-(1-\alpha)^{1/3}$
Diffusion			
One-way transport	D_1	0.5α	α^2
Two-way transport	D_2	$[-\ln(1-\alpha)]^{-1}$	$(1-\alpha)\ln(1-\alpha)+\alpha$
Three-way transport	D_3	$3/2(1-\alpha)^{2/3}[1-(1-\alpha)1/3]^{-1}$	$[1-(1-\alpha)^{1/3}]^2$
Ginstling-Brounshtein equation	D_4	$[1.5(1-\alpha)^{1/3}]^{-1}$	$(1–2\alpha/3)-(1-\alpha)^{2/3}$

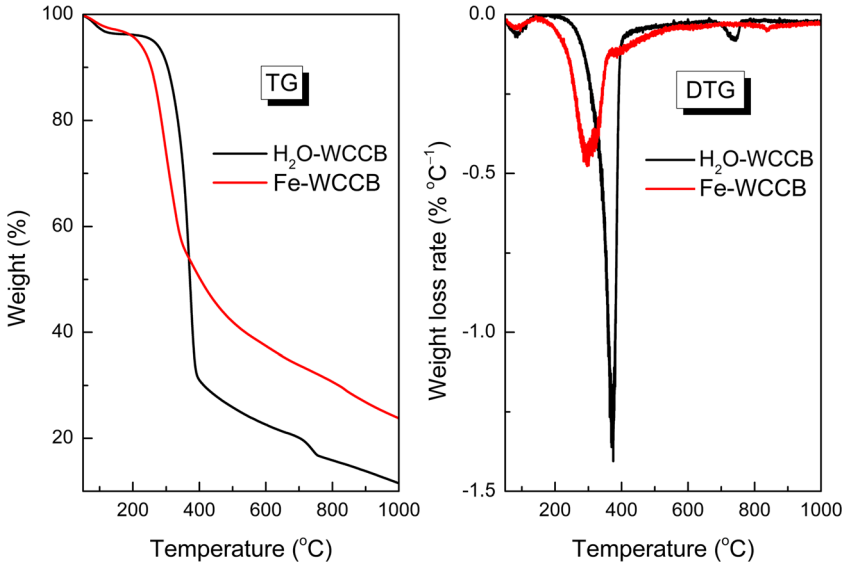

Fig. 3 TG and DTG curves of H_2O-WCCB and Fe-WCCB

reactions ended at 365 °C, indicating that the slurrying of WCCB using $FeCl_3$ solution was helpful for the occurrence of pyrolysis reactions at low temperatures. The DTG peak belonged to $CaCO_3$ disappeared due to the demineralization caused by H_3O^+ generated from the hydrolysis of $FeCl_3$ during slurrying [28]. It is worth noting that the solid residue rate of Fe-WCCB was as higher as 12.19% than that of WCCB at 1000 °C, indicating that Fe(III) loaded on WCCB greatly benefited the formation of char.

3.1.2 Pyrolysis kinetic

Pyrolysis kinetic parameters were determined by assuming single separate reaction for a particular stage of thermal decomposition. According to their DTG curves (Fig. 3), the main temperature ranges for pyrolysis of H_2O-WCCB and Fe-WCCB were selected. Equation (7) was applied separately to each of them, and a series of straight lines can be obtained by plotting $\ln[g(\alpha)/T^2)]$ versus $1/T$ using OriginPro 8.6 software (Fig. 4). The highest correlation coefficient (R^2) indicates that the corresponding reaction model reasonably fitted the experimental data. For the main pyrolysis stages of H_2O-WCCB and Fe-WCCB, D_1 and F_2 models had the highest R^2 values reached 0.9915 and 0.9943, respectively, and the change of reaction model suggested the change of pyrolysis reaction pathway. Moreover, the activation energies of the pyrolysis reactions of H_2O-WCCB and Fe-WCCB were calculated to be 129.59 and 52.96 kJ mol^{-1}, respectively. As known, cellulose was composed of numerous glucose units connected by glycosidic bonds, and the pyrolysis of cellulose is initiated from the cleavage of these glycosidic bonds [29].The break of glycosidic bonds can be facilitated through the attack of H_3O^+ generated from hydrolysis of $FeCl_3$ [28]. Moreover, as a typical Lewis acidic ion, Fe^{3+} possibly interacted with the glucose units during slurrying, forming relatively stable complexes and changing electronic cloud distribution; thus, the break of glycosidic bonds can be promoted [30, 31]. As a result, much less energy was needed for the thermal cracking of the cellulose in Fe-WCCB.

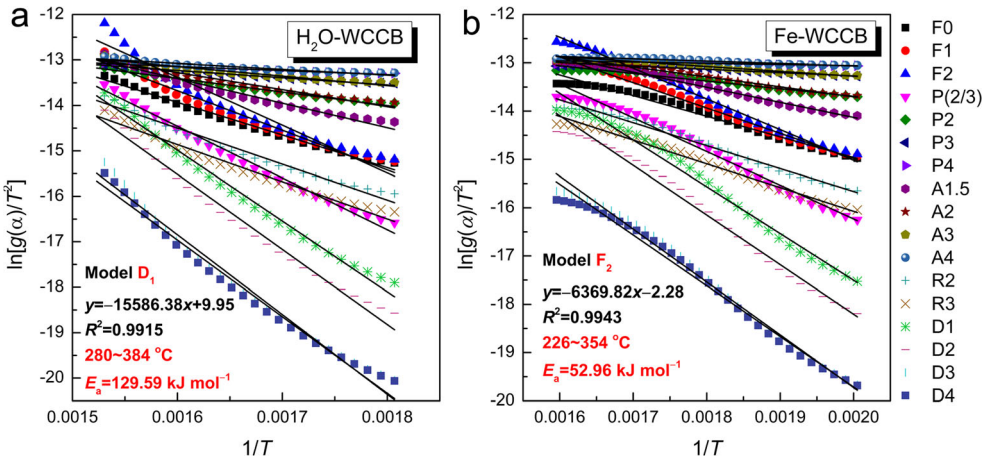

Fig. 4 Plots of $\ln[g(\alpha)/T^2]$ versus $1/T$ for pyrolysis of **a** H_2O-WCCB and **b** Fe-WCCB using different models

3.1.3 Analysis of gaseous products

The three-dimensional (3D) spectra (absorbance-wavenumber-temperature) of the volatiles produced from H_2O-WCCB and Fe-WCCB can be seen from Fig. 5 a and b, respectively. Gram-Schmidt curve indicates the variation of the yields of the volatile compounds with temperature. As shown in Fig. 5c, Gram-Schmidt curves H_2O-WCCB and Fe-WCCB had peaks at 368 and 322 °C, respectively, indicating the release of large amounts of gaseous products. When the temperature is fixed, absorbance information at different wavenumbers can be obtained to study the components released at this particular moment. Figure 5 d shows the FTIR spectra at the Gram-Schmidt peak temperatures for H_2O-WCCB and Fe-WCCB. The gaseous products composed of a variety of molecules were evolved due to the pyrolysis of cellulose. By comparing the spectra of H_2O-WCCB and Fe-WCCB, it was found that the types of the released products were not changed due to the presence of $FeCl_3$, but the relative contents of these components were changed. The peaks centered at 3575 and 1506 cm^{-1} represented –OH bond stretching vibrations in H_2O. The peak at 2819 cm^{-1} indicated the stretching vibration of C–H in acetaldehyde. The strongest peak at 2362 cm^{-1} was caused by the release of CO_2. The release of CO led to the presence of two subtle peaks at 2184 and 2113 cm^{-1}. The strong peak at 1748 cm^{-1} belonged to C=O stretching in furfurals. The peak at 1377 cm^{-1} can be ascribed to the bending vibration of phenolic –OH groups. The peaks at 1170 and 1106 cm^{-1} can be attributed to the stretching vibration of C–O–C in levoglucosan (LG) and –OH in hydroxyacetone (HA), respectively [32]. The subtle peak at 863 cm^{-1} suggested the presence of hydroxyacetaldehyde (HAA) [33].

The evolution histories of gaseous products from H_2O-WCCB and Fe-WCCB as a function of temperature are presented in Fig. 6. Basically, the release of gaseous products from Fe-WCCB started at lower temperatures, which was attributed to the destruction of cellulosic fibers by Fe^{3+} during slurrying, as mentioned in Sect. 3.1.2. More importantly, the yields of the volatiles significantly reduced due to the presence of Fe^{3+}, resulting in a higher char yield of Fe-WCCB. It was assumed that Fe(III) species played an important role in the inhibition of the generation of the volatile organics. The organics gaseous products were mainly released from Fe-WCCB between

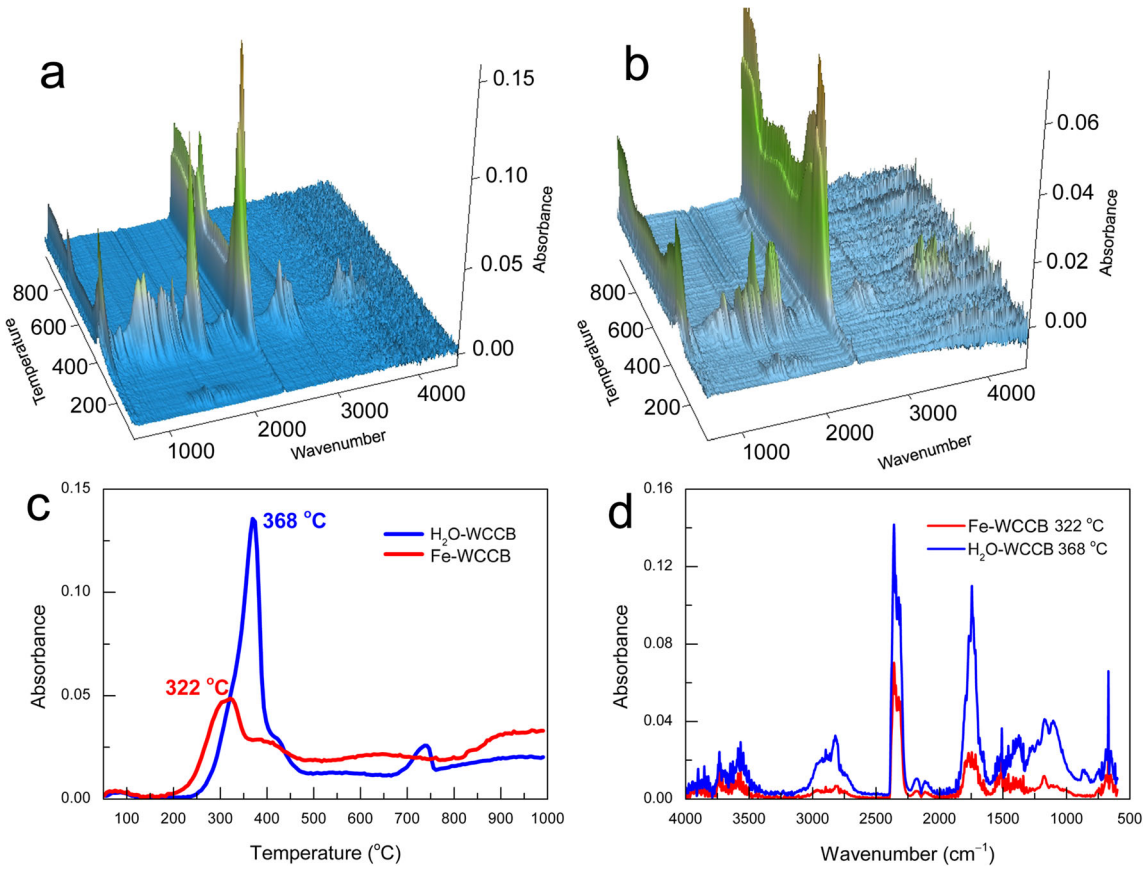

Fig. 5 3D spectra of volatiles produced from **a** H_2O-WCCB and **b** Fe-WCCB, **c** Gram-Schmidt curves H_2O-WCCB and Fe-WCCB, **d** FTIR spectra at the peak temperatures for H_2O-WCCB (368 °C) and Fe-WCCB (322 °C)

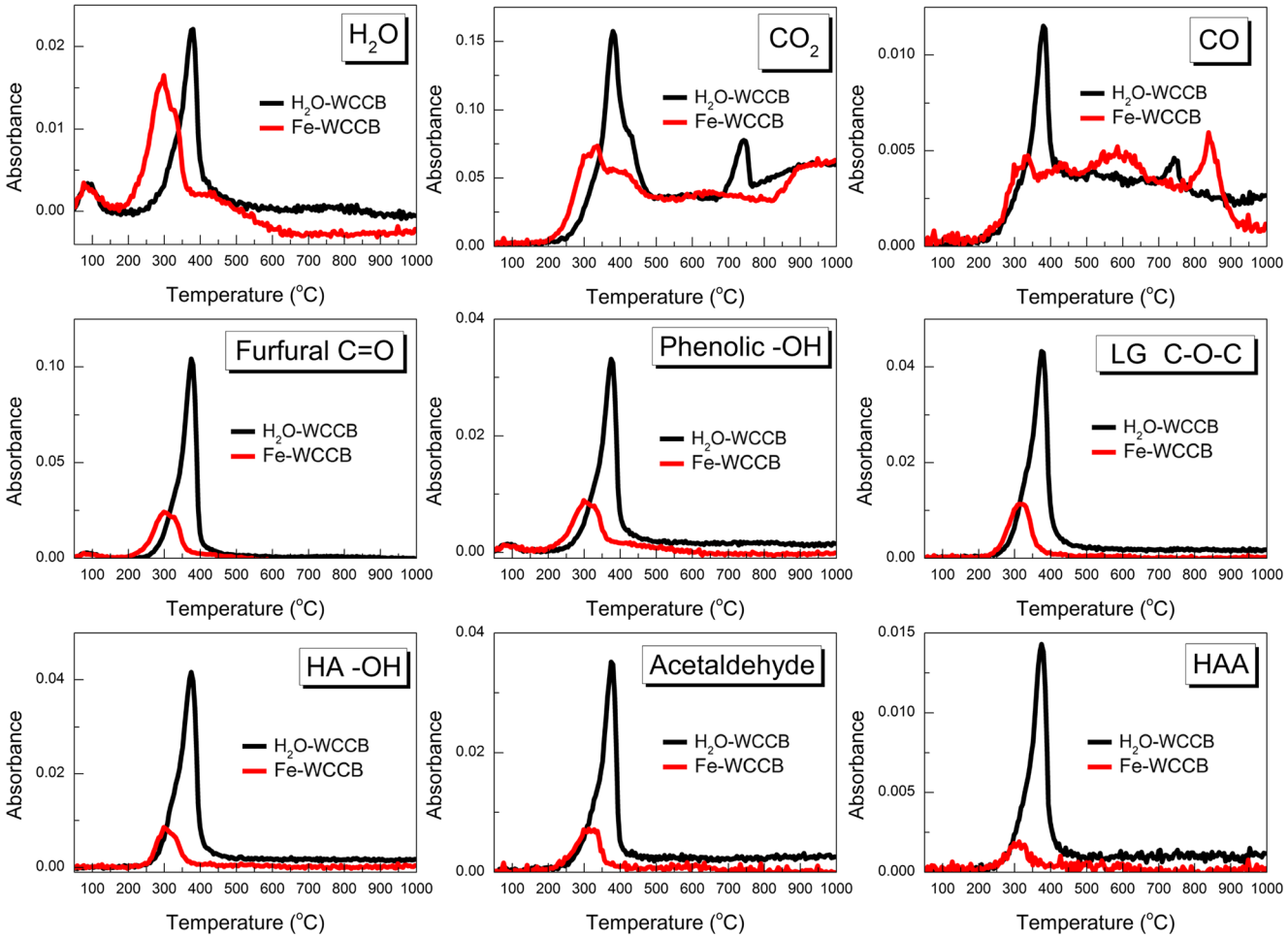

Fig. 6 Evolution histories of gaseous products from H_2O-WCCB and Fe-WCCB as a function of temperature

200 and 360 °C, and $FeCl_3$ decomposed into amorphous Fe(III) species (e.g., FeOOH) within this temperature range [34, 35].

$$FeCl_3 + 2H_2O \rightarrow FeOCl \cdot H_2O + 2HCl \rightarrow FeOOH + 3HCl \quad (8)$$

Many researchers suggested that the thermal conversion of cellulose follows free-radical mechanism [36–38]. It proposes that heat causes the vibration and cleavage of covalent bonds in cellulose, forming free radicals and radical terminals on the surface of the solid, and the reactions are not terminated till two radicals collide with each other to form stable compound [39, 40]. The stable gaseous products are mainly generated from the reactions between the hydrogen radical and other radicals in the gas phase, while the radical reactions occurred inside and on the surface of cellulose network result in the formation of char [41, 42]. It has been extensively reported that FeOOH or Fe_2O_3 can be used as a flame retardant and a smoke suppression agent, because Fe(III) has the ability to capture radicals generated via the thermal decomposition of polymers [43–47]. As illustrated in Fig. 7, instead of directly converting into stable gaseous products, the free radicals generated from the thermal cracking of WCCB were firstly trapped by the Fe(III) species deposited on the surface of the solid particles, enhancing the chances of these free radicals participating in char formation process via condensation and polymerization reactions. Thus, less gaseous products were released from Fe-WCCB and the char yield increased.

3.2 Characterization of porous carbon monolith

XRD patterns of $PCM_{Fe/300}$, $PCM_{Fe/400}$, $PCM_{Fe/500}$, $PCM_{Fe/600}$, $PCM_{Fe/700}$, and $PCM_{Fe/800}$ can be seen from Fig. 8. No Fe-related crystal structures (such as FeOOH, Fe_2O_3, Fe_3O_4) can be observed from XRD pattern of $PCM_{Fe/300}$, suggesting that Fe species in $PCM_{Fe/300}$ were in amorphous forms of short-range crystalline orders. The peak at 26.6 ° indicated the presence of quartz (SiO_2), which was used as a filler in WCCB [23]. For $PCM_{Fe/400}$, the peaks at 30.1°, 35.4°, 43.1°, 53.9°, 56.9°, and 62.8° corresponding to the (220), (311), (400), (422), (511), and (440) planes, respectively, confirmed the presence of magnetite (Fe_3O_4). With the carbonization

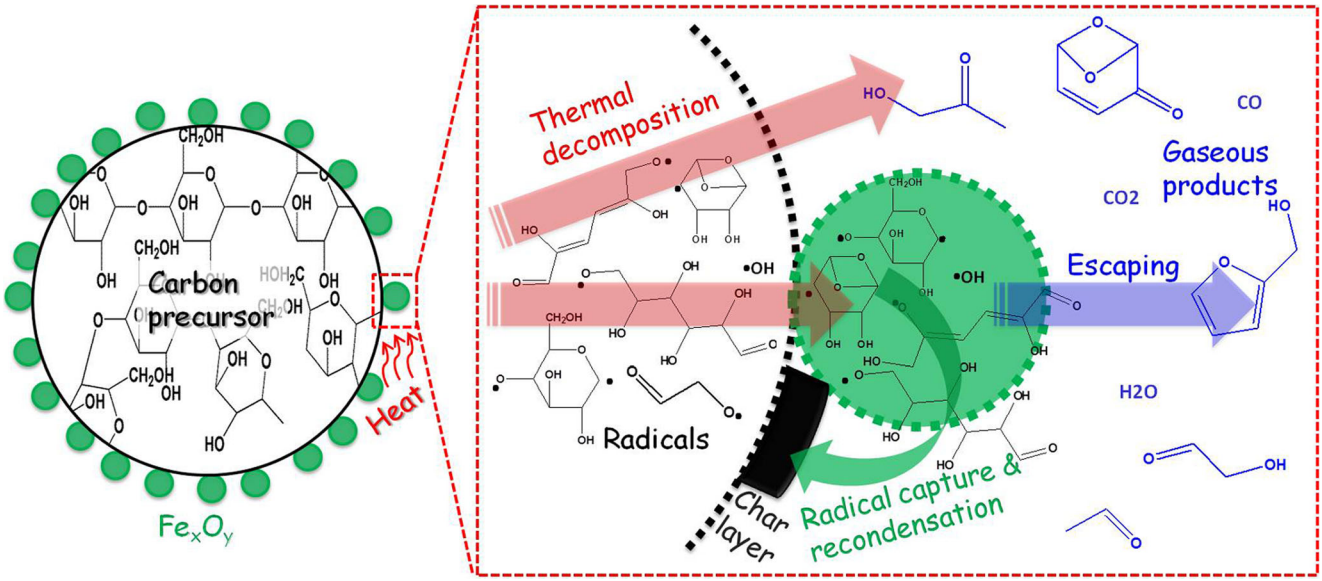

Fig. 7 Schematic diagram of thermal decomposition of Fe-WCCB

temperature increasing to 500, 600, and 700 °C, the intensity of Fe_3O_4 peaks continued to increase, indicating that higher carbonization temperature promoted the transformation of amorphous Fe species into crystalline Fe_3O_4. When the carbonization temperature achieved 800 °C, Fe_3O_4 peaks dramatically weakened and a sharp peak emerged at 44.8°, which belonged to (110) plane of α-Fe and proved the formation of zero-valent iron (Fe^0) due to the carbothermal reduction of Fe_3O_4. Unlike $PCM_{Fe/800}$, XRD pattern of PCM_{800} only had two peaks at 26.7° and 29.4° attributed to quartz (SiO_2) and calcite ($CaCO_3$), respectively.

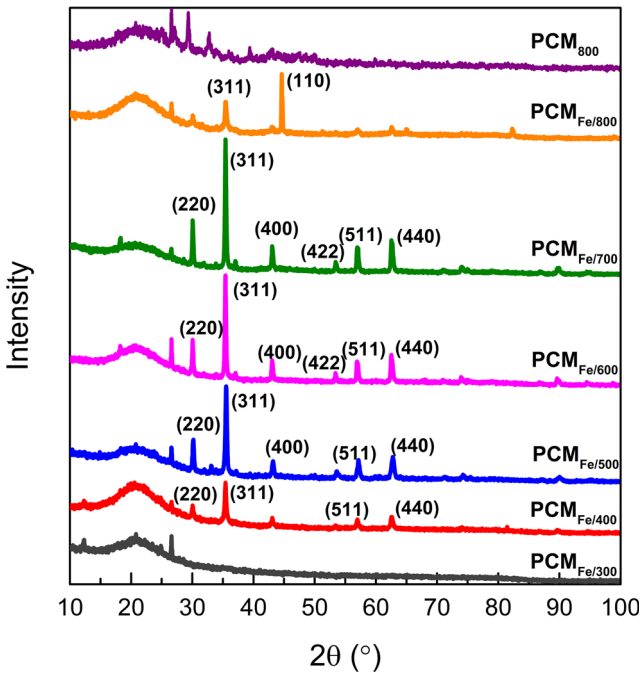

Fig. 8 XRD patterns of porous carbon monoliths

In fact, the transformation of Fe species and their interaction with WCCB-derived char can also be reflected by the evolution histories of CO and CO_2 from Fe-WCCB (see Fig. 6). The release of CO below 500 °C was caused by the thermal cracking of cellulose and the polymerization of the carbonaceous solid. The release of CO between 480 and 670 °C was possibly caused by the carbothermal reduction of the amorphous FeOOH or Fe_2O_3 by amorphous carbon [35, 48, 49].

$$6FeOOH + 4C \rightarrow 2Fe_3O_4 + 4CO \quad (9)$$

$$2FeOOH \rightarrow Fe_2O_3 + H_2O \quad (10)$$

$$3Fe_2O_3 + C \rightarrow 2Fe_3O_4 + CO \quad (11)$$

A sharp CO peak emerged at 840 °C, and the yield of CO_2 also ramped up above 820 °C. These phenomena can be explained by the reaction between Fe_3O_4 and amorphous carbon [34, 50].

$$Fe_3O_4 + 3C \rightarrow 3Fe + 2CO + CO_2 \quad (12)$$

Figure 9 shows the N_2-adsorption isotherm of $PCM_{Fe/400}$ within the relative pressure (P/P_0) range of 0 to 0.3, and N_2-adsorption/desorption isotherms of $PCM_{Fe/500}$, $PCM_{Fe/600}$, $PCM_{Fe/700}$, $PCM_{Fe/800}$, and PCM_{800} within the P/P_0 range of 0 to 1. The adsorption isotherms of all the samples except $PCM_{Fe/400}$ showed steep N_2 uptakes at $P/P_0 \leq 0.01$, suggesting the initial filling of micropores (pore diameter ≤ 2 nm). The adsorbed volumes increased gradually at $P/P_0 \geq 0.01$ with no plateau at high relative pressures, indicating the presence of mesopores (2 nm < pore diameter < 50 nm). Based on the N_2-adsorption data, the calculated value of BET surface area (S_{BET}) of $PCM_{Fe/400}$ was only 35 $m^2\ g^{-1}$, suggesting the incomplete removal of volatile matters at 400 °C. Pore characteristic parameters of the other samples calculated according

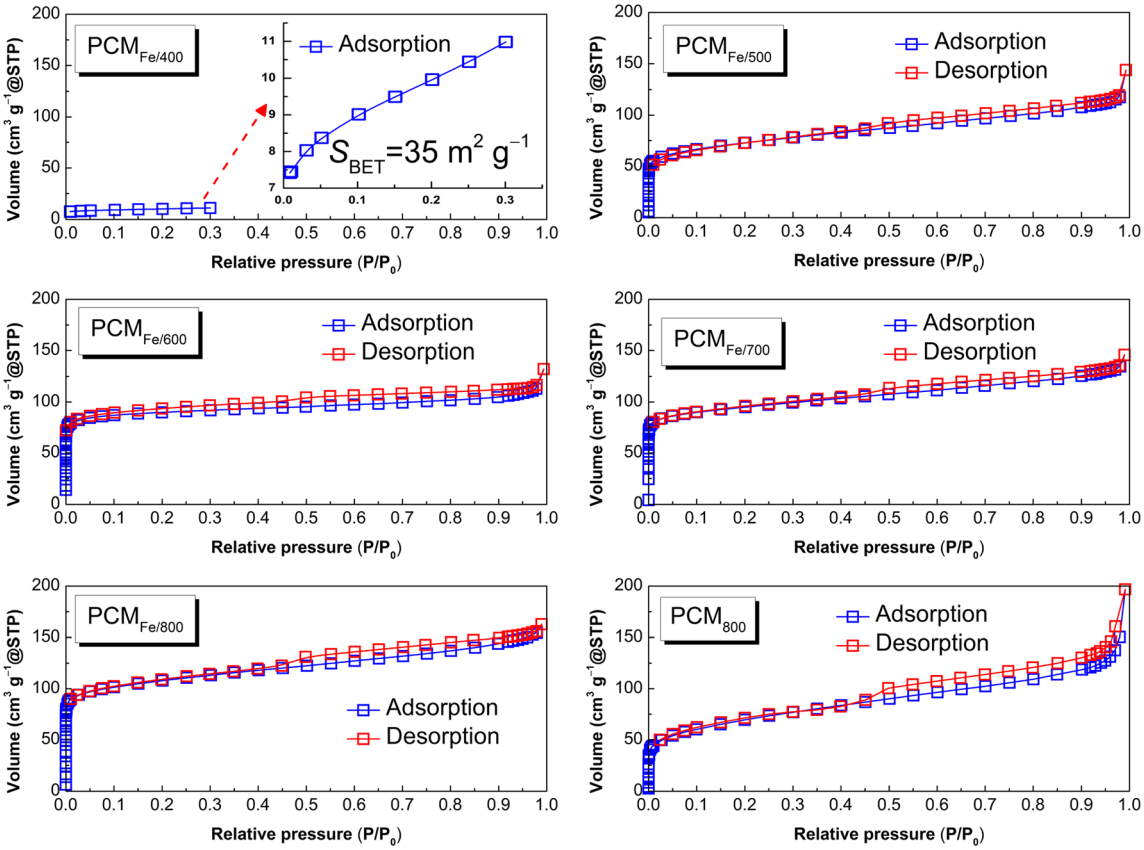

Fig. 9 N_2-adsorption/desorption isotherms of porous carbon monoliths

to the N_2-adsorption/desorption data are shown in Table 3. S_{BET} increased to 264 m^2 g^{-1} when the carbonization temperature reached up to 500 °C, because the releasing of volatiles at high temperature greatly favored the formation of pores. With the carbonization temperature increasing to 600 °C, higher micropore volume (V_{micro}) and S_{BET} were achieved due to the further removal of volatiles and consumption of amorphous carbon via the reduction of Fe(III) species to Fe_3O_4. The mesopore volume (V_{meso}) decreased because the sintering effect at high temperature resulting in the narrowing of pores and the shrinkage of carbon structure. The development of pore volume was affected slightly by the increase of carbonization temperature from 600 to 700 °C, because the releasing of volatiles finished within this temperature range, and only the consumption of amorphous carbon contributed to the development of porosity. S_{BET} increased remarkably from 358 to 404 m^2 g^{-1} because a lot of Fe_3O_4 formed below 800 °C was reduced to α-Fe, leading to the etching of char and formation of micropores. Compared with $PCM_{Fe/800}$, PCM_{800} had much lower S_{BET} and V_{micro}, but a higher V_{meso}. These differences demonstrated that the charring process of WCCB was significantly affected by $FeCl_3$, which was favorable to the formation of a more developed microporous structure. DFT pore size distribution of $PCM_{Fe/500}$, $PCM_{Fe/600}$, $PCM_{Fe/700}$, $PCM_{Fe/800}$, and PCM_{800} within different pore diameter ranges is shown in Fig. 10. $PCM_{Fe/500}$, $PCM_{Fe/600}$, $PCM_{Fe/700}$, and $PCM_{Fe/800}$ showed sharp peaks between 0.5 and 0.6 nm, indicating the presence of large amounts of micropores. Besides, more micropores with smaller diameters were formed with the carbonization temperature increasing from 500 to 800 °C. $PCM_{Fe/500}$, $PCM_{Fe/600}$, $PCM_{Fe/700}$, and $PCM_{Fe/800}$ also had mesopores with diameters between 2.25 and 4.30 nm. The distribution became weaker when the carbonization temperature increased from 500 to 600 °C

Table 3 Pore characteristics of porous carbon monoliths

Sample	S_{BET} (m^2 g^{-1})	V_{total} (cm^3 g^{-1})	V_{micro} (cm^3 g^{-1})	V_{meso} (cm^3 g^{-1})	D_{avg} (nm)	Diameter (cm)	Thickness (cm)	Yield (%)
$PCM_{Fe/500}$	264	0.222	0.109	0.125	3.37	1.51	0.49	40.94
$PCM_{Fe/600}$	351	0.205	0.137	0.065	2.33	1.42	0.45	38.38
$PCM_{Fe/700}$	358	0.225	0.143	0.092	2.51	1.40	0.44	37.70
$PCM_{Fe/800}$	404	0.252	0.163	0.098	2.49	1.37	0.40	35.08
PCM_{800}	247	0.304	0.101	0.226	4.94	1.31	0.38	20.37

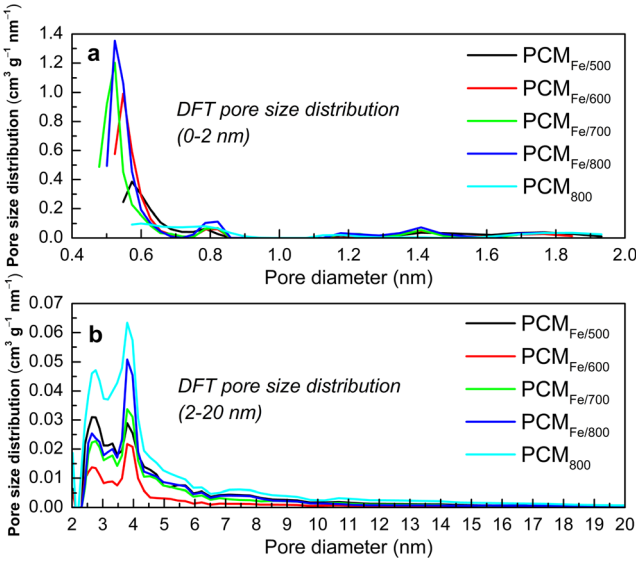

Fig. 10 DFT pore size distribution curves of porous carbon monoliths within pore diameter ranges of **a** 0–2 nm and **b** 2–20 nm

due to sintering effect, while the consumption of amorphous carbon contributed to the generation of some new mesopores within the same diameter range. By comparing the DFT curves of $PCM_{Fe/800}$ and PCM_{800}, it was found that the introduction of $FeCl_3$ was obviously beneficial to the formation of micropores. However, the mesoporous structure became less developed due to the blockage of mesopores caused by the $FeCl_3$-derived products.

As mentioned, carbon materials can be used as solar absorbers due to optical transitions in the D band. Thus, Raman spectrometry analysis was necessary [51]. Raman spectra of $PCM_{Fe/500}$, $PCM_{Fe/600}$, $PCM_{Fe/700}$, and $PCM_{Fe/800}$ are shown in Fig. 11a. The spectra of all the samples exhibited D band and G band centered at 1334 and 1580 cm^{-1}, respectively. D band is related to lattice defect and used to represent the disorder degree of graphite carbon, while G band is related to the vibration of sp^2-hybridized carbon atoms in a two-dimensional hexagonal lattice [52]. The ratio of the relative intensity of D band and G band (I_D/I_G) is proportional to the crystalline degree of carbon materials [53]. The I_D/I_G values of the samples increased from 0.74 to 0.97 with the carbonization temperature increasing from 500 to 800 °C, suggesting the presence of more defect sites. For a quantitative characterization of the samples, the UV-Vis-NIR spectra were measured in the broadband solar spectrum. As shown in Fig. 11b), $PCM_{Fe/600}$ exhibited high light absorption above 80% within a broadband wavelength from 256 to 2140 nm, demonstrating its highest solar light absorption ability among these samples. Although the lowest I_D/I_G value of $PCM_{Fe/500}$ suggested that this sample contained the most sp^2-hybridized carbon atoms and π electrons accounting for light absorption, $PCM_{Fe/600}$ and $PCM_{Fe/700}$ had higher light adsorption abilities than $PCM_{Fe/500}$. This was because the light adsorption ability of a porous carbon material was not only closely related with its π electrons, but also its pores. As shown in the inset, the incident light trapped in the pores of the carbon monolith can bounce back and forth between the walls, resulting in the light propagation and multiple light matter interactions and effective light harvest [4, 8, 54]. Thus, a higher BET surface area was no doubt conducive to improving the light adsorption.

The surface morphology of $PCM_{Fe/600}$ observed by SEM under different magnification is shown in Fig. 12. $PCM_{Fe/600}$ had an irregularly twisted fibrous network structure, with many open pores and gaps between the flat ribbon shaped and crisscrossed fibers, which enabled the capillary-induced water transport. It is worth to note that a lot of particles presenting on the surface of $PCM_{Fe/600}$, indicating the presence of Fe_3O_4. Under high magnification, it can be observed that the Fe_3O_4 particles had polyhedron structures, with the particle size ranging from tens of nanometers to about 1 μm. Besides, the Fe_3O_4 particles were partly embedded in the dent parts and wrinkled areas or deposited deeply in the gaps and pores, suggesting good mechanical bonding between the carbon matrix and magnetic particles.

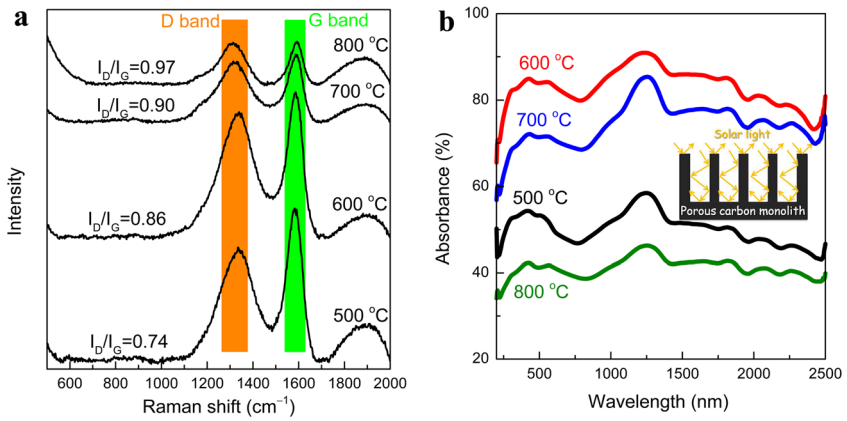

Fig. 11 **a** Raman and **b** UV-Vis-NIR spectra of porous carbon monoliths, the inset shows incident light trapped in the pores of porous carbon monolith bounces back and forth between the walls

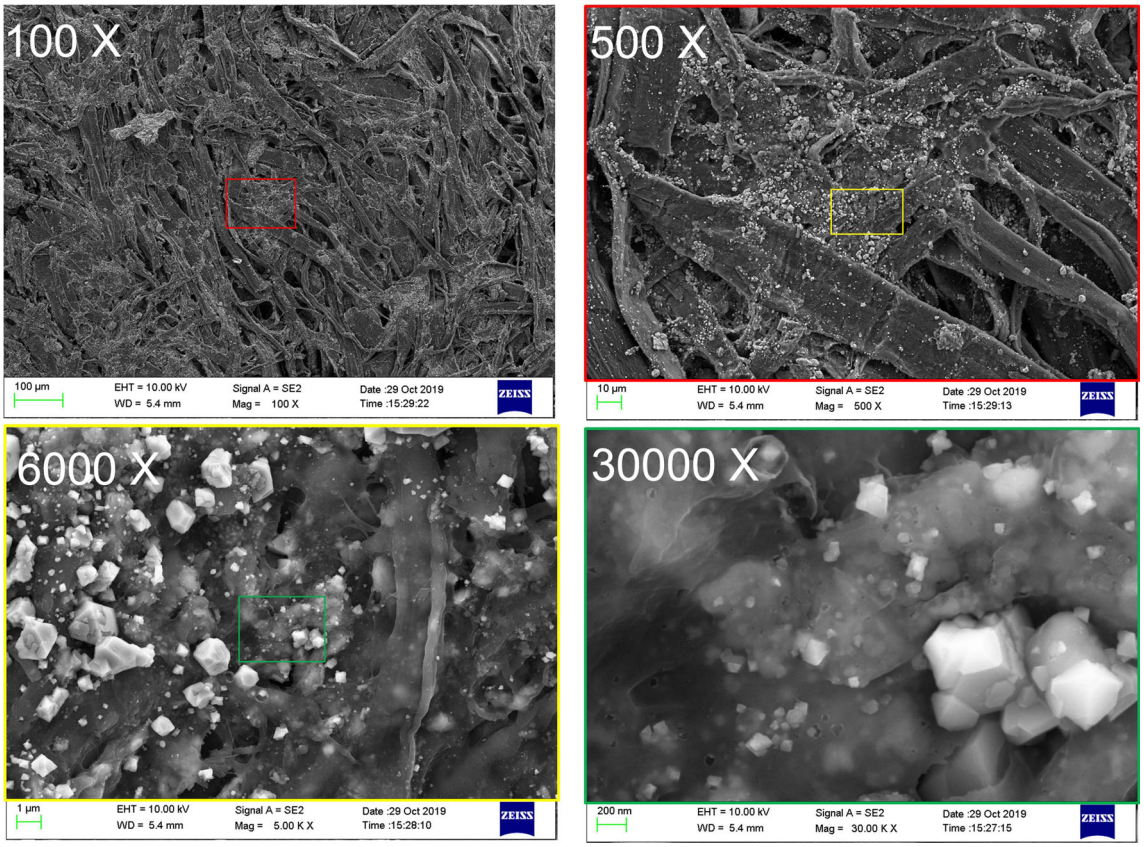

Fig. 12 Surface morphology of $PCM_{Fe/600}$ under different magnification

3.3 Photothermal conversion and solar steam generation tests

Since $PCM_{Fe/600}$ had the highest light adsorption ability among all the samples, and it was expected to exhibit excellent photothermal conversion performance. Thus, the study of photothermal activity was focused on $PCM_{Fe/600}$. Surface temperature measurement under a certain intensity of solar irradiation is widely used to evaluate the light-to-heat conversion performance of photothermal materials [55]. The variation of the recorded temperature of $PCM_{Fe/600}$ surface with irradiation time can be seen from Fig. 13, and the inset shows the optical image of $PCM_{Fe/600}$ being irradiated under 0.25 sun and the IR images of $PCM_{Fe/600}$ surface under 0.25 sun irradiation for 1830 s in the dry state. The surface temperature of $PCM_{Fe/600}$ increased rapidly from 25.2 to 51.6 °C within the first 60 s. The increase of temperature became slowly after 150 s, and finally attained a high equilibrium value (61.9 °C) within 1830 s. The temperature variation proved that $PCM_{Fe/600}$ had a good photothermal conversion performance, implying it can be used as a promising candidate of SSG.

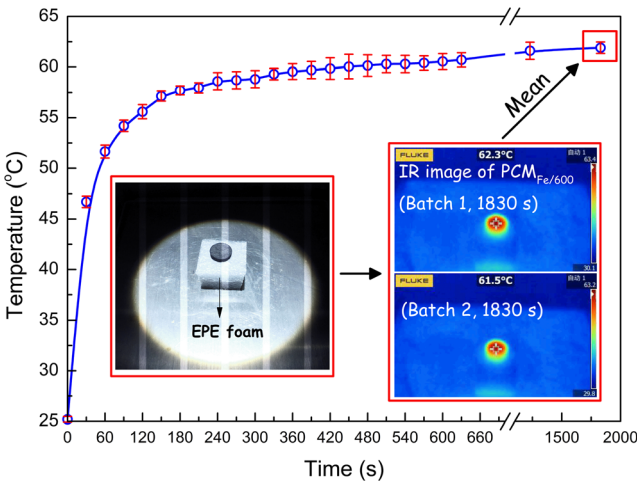

Fig. 13 Variation of temperature of $PCM_{Fe/600}$ surface with irradiation time, the inset shows the optical image of $PCM_{Fe/600}$ being irradiated under 0.25 sun and the IR images of $PCM_{Fe/600}$ surface under 0.25 sun irradiation for 1830 s in the dry state

Mechanical stability is important during the use of the monolith for SSG, because the easy destruction of the samples must be avoided. As shown in Fig. 14, $PCM_{Fe/600}$ was pressed under a beaker filled with water weighing 1267.75 g, and the monolith character of $PCM_{Fe/600}$ can be perfectly retained. This proved that $PCM_{Fe/600}$ was

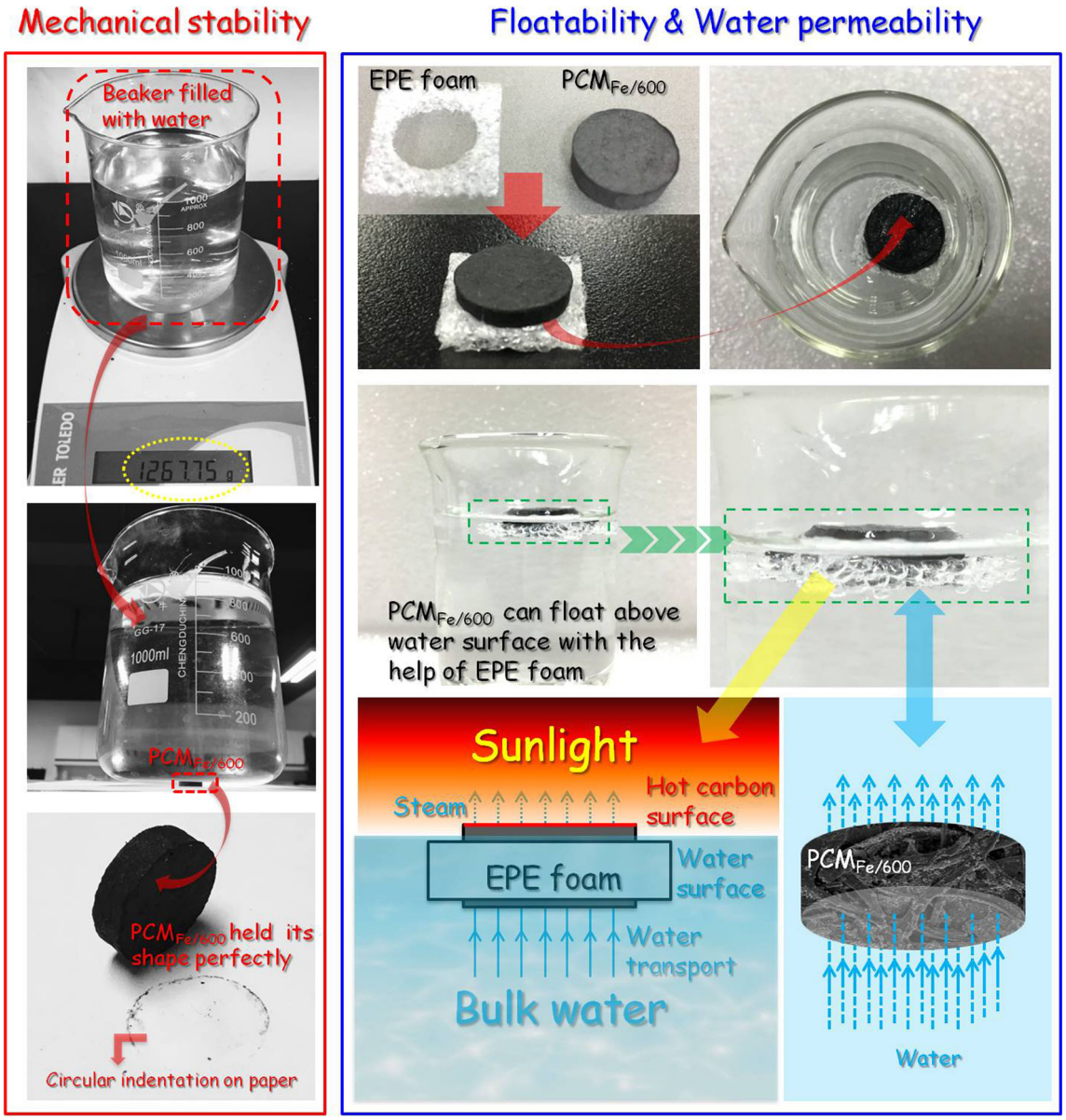

Fig. 14 Optical images of $PCM_{Fe/600}$ being pressed under a beaker filled with water and floating on water surface and schematic diagram of $PCM_{Fe/600}$-based interfacial solar steam generation platform

able to withstand the pressure at least 4875 times of its own weight (2.55 N), thus we can say that $PCM_{Fe/600}$ had a good mechanical rigidity. Moreover, $PCM_{Fe/600}$ can float well just above the water surface with the help of EPE foam. A hot region is expected to appear on the top of $PCM_{Fe/600}$ under solar irradiation via photothermal conversion. Benefitting from the porous framework providing water transport channels, water can be continuously pumped to the hot upper surface of $PCM_{Fe/600}$. In this configuration, the solar energy is localized at the water-air interface to heat thin layer where evaporation occurs, instead of wastefully heating the entire body of water, which conforms to the definition of interfacial SSG (ISSG) [3, 56].

Figure 15 a shows the photographs of the two different steam generation scenes (the temperature measuring points were marked by "+") and the IR images of the floating $PCM_{Fe/600}$, water surrounding $PCM_{Fe/600}$ and pure water under 0.25 sun irradiation for 3600 s. Figure 15 b shows the variation of temperature of the floating $PCM_{Fe/600}$ surface, neighboring water of $PCM_{Fe/600}$ and pure water with irradiation time. The temperature of $PCM_{Fe/600}$ surface rapidly increased from 22.7 to 31.7 °C within 300 s, and slowly increased to 36.5 °C

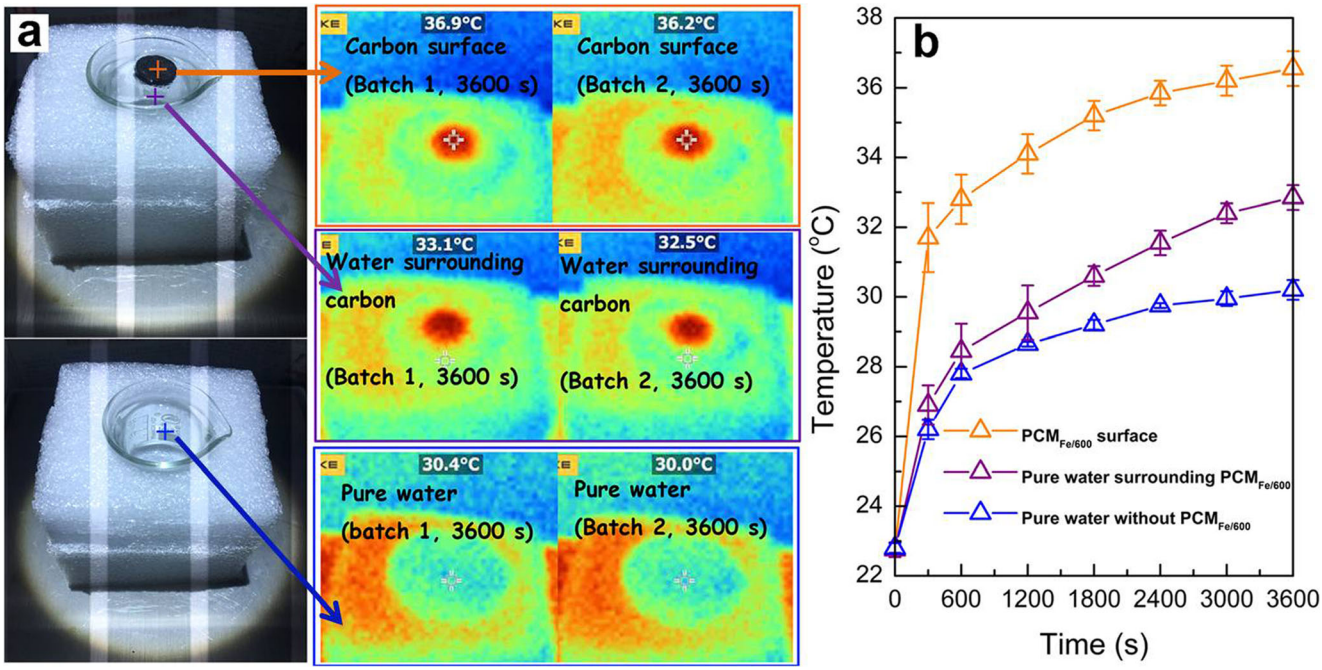

Fig. 15 **a** Photographs of two different steam generation scenes and the IR images of the floating $PCM_{Fe/600}$, water surrounding $PCM_{Fe/600}$ and pure water under 0.25 sun irradiation for 3600 s. **b** Variation of surface temperature of floating $PCM_{Fe/600}$, neighboring water of $PCM_{Fe/600}$ and pure water with irradiation time

over the remaining time. Meanwhile, the surface temperature of the neighboring water of $PCM_{Fe/600}$ reached 32.9 °C within 3600 s, while that of pure water increased to 30.2 °C. The results proved that the top of the floating $PCM_{Fe/600}$ was able to become a hot layer for generating steam. Besides, the neighboring water surface can be heated due to heat transfer from $PCM_{Fe/600}$. Figure 16 shows that the evaporation of pure water within 3600 s was 0.37 g, while the evaporation of water in the presence of the floating $PCM_{Fe/600}$ increased to 0.54 g under the same condition. The increase in water evaporation can be attributed to ISSG occurred on the hot surface of $PCM_{Fe/600}$. Moreover, as shown in the inset, $PCM_{Fe/600}$ acted as the heat source distributing heat to the neighboring water, thus this heat island effect no doubt contributed to the improvement of steam generation.

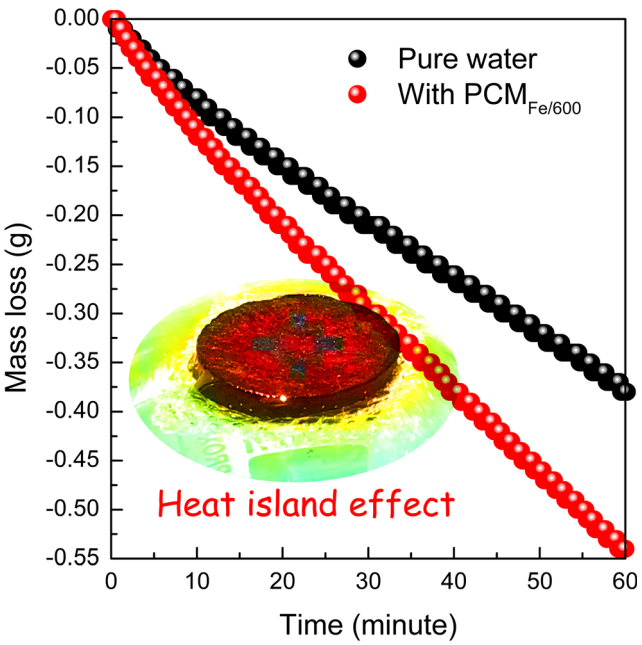

Fig. 16 Mass loss of water with and without $PCM_{Fe/600}$ at various time points

3.4 Adsorption study

Based on the above experiments, $PCM_{Fe/600}$ was proved to be an excellent photothermal material and able to promote SSG by interface evaporation and heat island effects. To determine whether $PCM_{Fe/600}$ was simultaneously suitable for SSG and adsorption, the adsorption behavior of $PCM_{Fe/600}$ for MB was studied. The adsorption isotherm of MB on $PCM_{Fe/600}$ is shown in Fig. 17a, as can be seen, the increase in initial concentration of MB led to the increase of adsorption equilibrium, this was because the initial concentration provided a driving force for MB transferred from the aqueous phase to the surface of $PCM_{Fe/600}$. The inset of Fig. 17a shows the linear fitting of adsorption equilibrium data by Langmuir, Freundlich and Temkin isotherm models, and the best fitting model can be determined by the highest R^2 value. R^2 values and the isotherm

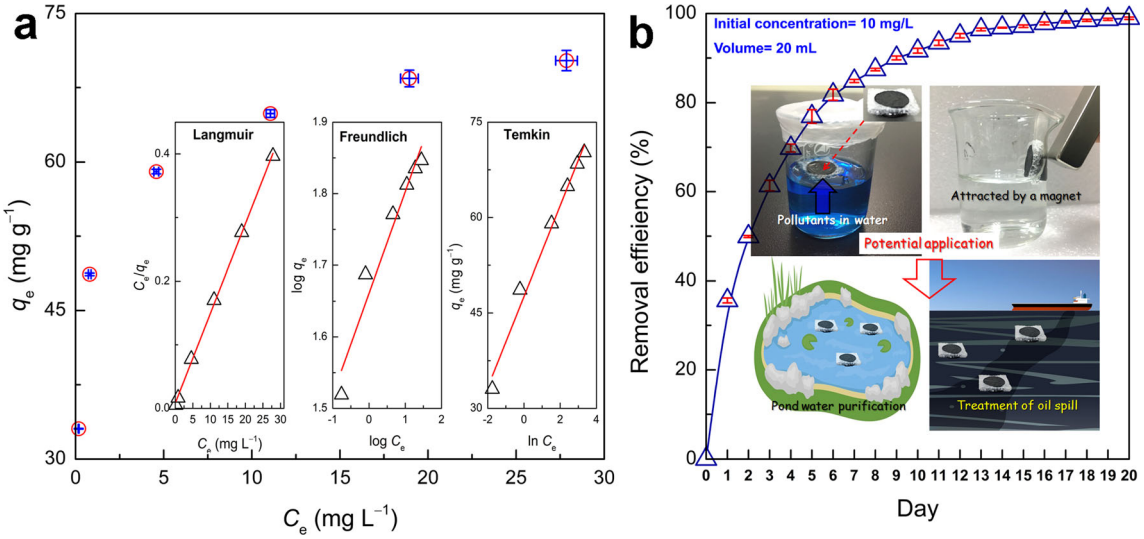

Fig. 17 **a** Adsorption isotherm of MB on powdered $PCM_{Fe/600}$, the inset shows linear fitting of equilibrium isotherm data by Langmuir, Freundlich and Temkin isotherm models. **b** Variation of MB concentration in the presence of floating $PCM_{Fe/600}$ with contact time, the inset shows the optical images of $PCM_{Fe/600}$ floating on surface of MB solution and $PCM_{Fe/600}$ being attracted by a magnet, and the schematic diagrams of potential applications of $PCM_{Fe/600}$

parameters calculated from the slopes and intercepts can be seen in Table 4. Langmuir model had the best fitting, suggesting the formation of MB monolayer on the $PCM_{Fe/600}$ surface and no further adsorption occurred after the formation of the monolayer, and there was no MB molecules transmigrated in the plane of the neighboring surface. Moreover, each MB molecule had similar enthalpy and activation energy. Based on the Langmuir constant, the maximum monolayer adsorption capacity of $PCM_{Fe/600}$ for MB was calculated to be 70.9 mg g^{-1}. The comparison of MB adsorption capacities of $PCM_{Fe/600}$ and some other waste-derived porous carbon materials are shown in Table 5. As can be seen, $PCM_{Fe/600}$ showed a competitive MB adsorption capacity, outperforming some other porous carbons in the literatures.

To simulate the process of the purification of natural water body using a floating absorbent, $PCM_{Fe/600}$ embedded in EPE foam was put into a beaker containing 20 mL of MB aqueous solution with the initial concentration of 10 mg L^{-1}. $PCM_{Fe/600}$ kept floating on water surface with the help of EPE foam, then the beaker was sealed using parafilm and left undisturbed. As shown in Fig. 17b, the removal efficiency of MB by $PCM_{Fe/600}$ reached 77% within 5 days, and it continued to increase smoothly to nearly 100% on day 20. The adsorption rate was not as fast as that of a floatable carbon monoliths reported in a previous study [62, 67], and this was possibly because of the following reasons. First, $PCM_{Fe/600}$ needed more macro- and mesopores that provided channels for the fast diffusion of the MB dye to the active adsorption sites. Second, a stronger interaction between the functional groups on $PCM_{Fe/600}$ surface and MB molecules was required. Third, in the present study, the low initial concentration of MB solution provided limited driving force for mass transfer between the aqueous phase and solid medium. Besides, the MB solution was left undisturbed without stirring that can increasing contact between MB and $PCM_{Fe/600}$. The deficiencies of $PCM_{Fe/600}$ are pointed out, as well as the future research directions. Anyway, the floating $PCM_{Fe/600}$ was proved to be useful for absorbing the dissolved pollutants from water. Moreover, As can be seen from the inset, the MB-absorbed $PCM_{Fe/600}$ can be recovered from water via magnetic separation, and this phenomenon also reflected the potential of the floating $PCM_{Fe/600}$ being manipulated by magnetic force during its use. Based on the adsorption ability and magnetic response exhibited by the floating $PCM_{Fe/600}$, this material may find applications in pond water purification and environmental clean-up of oil spills.

Table 4 Fitting parameters for Langmuir, Freundlich, and Temkin isotherm model

Langmuir			Freundlich			Temkin		
q_m	K_L	R^2	K_F	n	R^2	A_T	B_T	R^2
70.9	1.72	0.9987	45.79	7.05	0.9446	7.83×10^2	7.14	0.9841

4 Conclusion

Porous carbon monoliths were prepared from waste corrugated cardboard box (WCCB) via slurrying in $FeCl_3$

Table 5 Comparison of MB adsorption capacities of various waste-derived porous carbons

Adsorbent	Raw material	Adsorption capacity (mg g^{-1})	Ref.
Activated biochar	Barley malt bagasse	161	[57]
Pyrolytic carbon	Waste tires	71.6	[58]
HNO_3-treated biochar	Reed	33.33	[59]
Activated carbon	Cocoa pod husk	109.9	[60]
Biochar	Pig manure	53.67	[61]
Porous carbon monolith	Sugarcane bagasse scaffold	101	[62]
Biochar	Sewage sludge	29.85	[63]
Micro-mesoporous carbon	Cotton waste	68.70	[64]
Biochar	Date seed	42.57	[65]
Carbon fiber aerogel	Abandoned cotton	102.23	[66]
$PCM_{Fe/600}$	Waste corrugated cardboard box	70.9	This study

solution, molding, and carbonization. $FeCl_3$ was helpful for the pyrolysis of WCCB at lower temperatures, and the activation energy was reduced by 76.63 kJ mol^{-1} because Lewis acidic Fe^{3+} promoted the breaking of glycosidic bonds of cellulose contained in WCCB. $FeCl_3$ was also beneficial to char formation because the radicals released from WCCB during pyrolysis can be captured by Fe(III) species derived from $FeCl_3$. Amorphous Fe(III) species in PCMs continuously converted into crystalline Fe_3O_4 when the carbonization temperature increased from 400 to 700 °C, and the carbothermal reduction of Fe_3O_4 at 800 °C led to the formation of α-Fe. Both the release of volatiles and etching of carbon contributed to the development of the porous structure of PCMs, and $FeCl_3$ was favorable to the formation of micropores. The optimal sample ($PCM_{Fe/600}$) exhibited high optical absorption above 80% within a broadband wavelength, because it was rich in both sp^2-hybridized carbon atoms and pores. The surface temperature of $PCM_{Fe/600}$ in dry state achieved 61.9 °C under 0.25 sun irradiation due to its good photothermal conversion ability. $PCM_{Fe/600}$-assisted water evaporation was 1.46 times that of the pure water because of the occurrence of interfacial solar-derived evaporation and heat island effect. Methylene blue can be effectively absorbed from water by $PCM_{Fe/600}$ floating on water surface, and the adsorption equilibrium data of $PCM_{Fe/600}$ for MB followed Langmuir model with a monolayer adsorption capacity of 70.9 mg g^{-1}.

Acknowledgments This work was financially supported by the National Natural Science Foundation of China (51909292) and Fundamental Research Funds for Central Public Welfare Scientific Research Institution (K-JBYWF-2019-ZT02, Y-JBYWF-2019-16). The authors wish to thank the anonymous reviewers for their comments. This paper was wrote when COVID-19 pandemic was raging in China, the authors sincerely thank the medical workers and people from all walks of life who have been fighting in the frontline to maintain the normal operation of society.

References

1. Lin Y, Xu H, Shan X, Di Y, Zhao A, Hu Y, Gan Z (2019) Solar steam generation based on the photothermal effect: from designs to applications, and beyond. J Mater Chem A 7:19203–19227
2. Cavusoglu AH, Chen X, Gentine P, Sahin O (2017) Potential for natural evaporation as a reliable renewable energy resource. Nat Commun 8:617
3. Zhu L, Gao M, Peh CKN, Ho GW (2019) Recent progress in solar-driven interfacial water evaporation: advanced designs and applications. Nano Energy 57:507–518
4. Wang P (2018) Emerging investigator series: the rise of nano-enabled photothermal materials for water evaporation and clean water production by sunlight. Environ Sci: Nano 5:1078–1089
5. Wang Z, Horseman T, Straub A P, Yip N Y, Li D, Elimelech M, Lin S (2019) Pathways and challenges for efficient solar-thermal desalination. Sci Adv 5: eaax0763
6. Zhang Q, Xu W, Wang X (2018) Carbon nanocomposites with high photothermal conversion efficiency. Sci China Mater 61:905–914
7. Sun L, Liu J, Zhao Y, Xu J, Li Y (2019) Highly efficient solar steam generation via mass-produced carbon nanosheet frameworks. Carbon 145:352–358
8. Ma S, Qarony W, Hossain MI, Yip CT, Tsang YH (2019) Metal-organic framework derived porous carbon of light trapping structures for efficient solar steam generation. Sol Energ Mat Sol C 196: 36–42
9. Liu F, Zhao B, Wu W, Yang H, Ning Y, Lai Y, Bradley R (2018) Low cost, robust, environmentally friendly geopolymer-mesoporous carbon composites for efficient solar powered steam generation. Adv Funct Mater 28:1803266
10. Liu D, Deng S, Maimaiti A, Wang B, Huang J, Wang Y, Yu G (2018) As(III) and As(V) adsorption on nanocomposite of hydrated zirconium oxide coated carbon nanotubes. J Colloid Interface Sci 511:277–284
11. Huggins TM, Haeger A, Biffinger JC, Ren ZJ (2016) Granular biochar compared with activated carbon for wastewater treatment and resource recovery. Water Res 94:225–232
12. Fan S, Zhang L (2019) Production and characterization of tea waste–based biochar and its application in treatment of Cd-containing wastewater. Biomass Conv Bioref. https://doi.org/10.1007/s13399-019-00545-8

13. Liu S, Pan M, Feng Z, Qin Y, Wang Y, Tan L, Sun T (2020) Ultra-high adsorption of tetracycline antibiotics on garlic skin-derived porous biomass carbon with high surface area. New J Chem 44: 1097–1106
14. Qi C, Xu L, Zhang M, Zhang M (2019) Fabrication and application of hierarchical porous carbon for the adsorption of bulky dyes. Microporous Mesoporous Mater 290:109651
15. Jamil S, Loganathan P, Listowski A, Kandasamy J, Khourshed C, Vigneswaran S (2019) Simultaneous removal of natural organic matter and micro-organic pollutants from reverse osmosis concentrate using granular activated carbon. Water Res 155:106–114
16. Fu M, Chen W, Zhu X, Yang B, Liu Q (2019) Crab shell derived multi-hierarchical carbon materials as a typical recycling of waste for high performance supercapacitors. Carbon 141:748–757
17. Fu M, Chen W, Ding J, Zhu X, Liu Q (2019) Biomass waste derived multi-hierarchical porous carbon combined with CoFe2O4 as advanced electrode materials for supercapacitors. J Alloys Compd 782:952–960
18. Lua AC (2019) A detailed study of pyrolysis conditions on the production of steam-activated carbon derived from oil-palm shell and its application in phenol adsorption. Biomass Conv Bioref. https://doi.org/10.1007/s13399-019-00447-9
19. Cuong DV, Liu NL, Nguyen VA, Hou CH (2019) Meso/micropore-controlled hierarchical porous carbon derived from activated biochar as a high-performance adsorbent for copper removal. Sci Total Environ 692:844–853
20. Mozaffarian M, Soleimani M, Bajgiran MA (2019) A simple novel route for porous carbon production from waste tyre. Environ Sci Pollut R 26:31038–31054
21. Yuan S-J, Zhang J-J, Fan H-X, Dai X-H (2018) Facile and sustainable shear mixing/carbonization approach for upcycling of carton into superhydrophobic coating for efficient oil-water separation. J Clean Prod 196:644–652
22. Yi Y, Wang Z, Wennersten R, Sun Q (2017) Life cycle assessment of delivery packages in China. Energy Procedia 105:3711–3719
23. Ding Z, Xu X, Phan T, Hu X (2018) Carbonized waste corrugated paper packaging boxes as low-cost adsorbent for removing aqueous Pb(II), Cd(II), Zn(II), and methylene blue. Pol J Environ Stud 27: 2483–2491
24. Lykidis C, Parnavela C, Goulounis N, Grigoriou A (2012) Potential for utilizing waste corrugated paper containers into wood composites using UF and PMDI resin systems. Euro J Wood Prod 70:811–818
25. Liu Y, Yan C, Zhang Z, Gong Y, Wang H, Qiu X (2016) A facile method for preparation of floatable and permeable fly ash-based geopolymer block. Mater Lett 185:370–373
26. Cao J, Ma Y (2019) Pyrolysis and gasification of macroalgae *Enteromorpha prolifera* under a CO_2 atmosphere using the thermogravimetry–Fourier transform infrared spectroscopy technique. Prog React Kinet Mech 44:132–142
27. Ma Y, Wang J, Zhang Y (2017) TG–FTIR study on pyrolysis of waste printing paper. J Therm Anal Calorim 129:1225–1232
28. Di Fidio N, Antonetti C, Raspolli Galletti AM (2019) Microwave-assisted cascade exploitation of giant reed (*Arundo donax L.*) to xylose and levulinic acid catalysed by ferric chloride. Bioresour Technol 293:122050
29. Nishimura M, Iwasaki S, Horio M (2009) The role of potassium carbonate on cellulose pyrolysis. J Taiwan Inst Chem E 40:630–637
30. Qiao Y, Pedersen CM, Huang D, Ge W, Wu M, Chen C, Jia S, Wang Y, Hou X (2016) NMR study of the hydrolysis and dehydration of inulin in water: comparison of the catalytic effect of Lewis acid $SnCl_4$ and Brønsted acid HCl. ACS Sustain Chem Eng 4: 3327–3333
31. Amarasekara AS, Deng F (2019) Single reagent treatment and degradation of switchgrass using iron(III)chloride: the effects on hemicellulose, cellulose and lignin. Biomass Bioenergy 131:105421
32. Wang S, Guo X, Wang K, Luo Z (2011) Influence of the interaction of components on the pyrolysis behavior of biomass. J Anal Appl Pyrolysis 91:183–189
33. Liu Q, Zhong Z, Wang S, Luo Z (2011) Interactions of biomass components during pyrolysis: a TG-FTIR study. J Anal Appl Pyrolysis 90:213–218
34. Xu Z, Zhou Y, Sun Z, Zhang D, Huang Y, Gu S, Chen W (2020) Understanding reactions and pore-forming mechanisms between waste cotton woven and $FeCl_3$ during the synthesis of magnetic activated carbon. Chemosphere 241:125120
35. Zhu X, Qian F, Liu Y, Matera D, Wu G, Zhang S, Chen J (2016) Controllable synthesis of magnetic carbon composites with high porosity and strong acid resistance from hydrochar for efficient removal of organic pollutants: an overlooked influence. Carbon 99:338–347
36. Mettler MS, Mushrif SH, Paulsen AD, Javadekar AD, Vlachos DG, Dauenhauer PJ (2012) Revealing pyrolysis chemistry for biofuels production: conversion of cellulose to furans and small oxygenates. Energy Environ Sci 5:5414–5424
37. Zhang X, Yang W, Blasiak W (2012) Kinetics of levoglucosan and formaldehyde formation during cellulose pyrolysis process. Fuel 96:383–391
38. He W, Liu Q, Shi L, Liu Z, Ci D, Lievens C, Guo X, Liu M (2014) Understanding the stability of pyrolysis tars from biomass in a view point of free radicals. Bioresour Technol 156:372–375
39. Volpe R, Bermudez Menendez JM, Ramirez Reina T, Volpe M, Messineo A, Millan M, Titirici M-M (2019) Free radicals formation on thermally decomposed biomass. Fuel 255:115802
40. Liu W-J, Jiang H, Yu H-Q (2015) Development of biochar-based functional materials: toward a sustainable platform carbon material. Chem Rev 115:12251–12285
41. Liu Z (2014) Frontiers and challenges of coal chemistry: structure and reaction. Sci Sin Chim 44:1431–1438 (In Chinese)
42. Zhang P, Hu H, Tang H, Yang Y, Liu H, Lu Q, Li X, Worasuwannarak N, Yao H (2019) In-depth experimental study of pyrolysis characteristics of raw and cooking treated shrimp shell samples. Renew Energy 139:730–738
43. Marinović-Cincović M, Popović MČ, Novaković MM, Nedeljković JM (2007) The influence of β-FeOOH nanorods on the thermal stability of poly(methyl methacrylate). Polym Degrad Stab 92:70–74
44. Liu L, Zhuo J, Chen X, Jiao C, Li S, Gu Y (2014) Influence of ferric hydroxide on smoke suppression properties and combustion behavior of intumescent flame retardant silicone rubber composites. J Therm Anal Calorim 119:487–497
45. Chen X, Liu L, Jiao C (2015) Influence of iron oxide brown on smoke-suppression properties and combustion behavior of intumescent flame-retardant epoxy composites. Adv Polym Technol 34: 21516
46. Chen X, Jiang Y, Jiao C (2014) Smoke suppression properties of ferrite yellow on flame retardant thermoplastic polyurethane based on ammonium polyphosphate. J Hazard Mater 266:114–121
47. Wang W, Pan H, Shi Y, Pan Y, Yang W, Liew KM, Song L, Hu Y (2016) Fabrication of LDH nanosheets on β-FeOOH rods and applications for improving the fire safety of epoxy resin. Compos Part A: Appl S 80:259–269
48. Dai SJ, Zhao YC, Niu DJ, Li Q, Chen Y (2019) Preparation and reactivation of magnetic biochar by molten salt method: relevant performance for chlorine-containing pesticides abatement. J Air Waste Manage Assoc 69:58–70
49. Xu Z, Sun Z, Zhou Y, Chen W, Zhang T, Huang Y, Zhang D (2019) Insights into the pyrolysis behavior and adsorption properties of activated carbon from waste cotton textiles by $FeCl_3$-activation. Colloid Surface A 582:123934
50. Pereira MC, Coelho FS, Nascentes CC, Fabris JD, Araujo MH, Sapag K, Oliveira LC, Lago RM (2010) Use of activated carbon

as a reactive support to produce highly active-regenerable Fe-based reduction system for environmental remediation. Chemosphere 81: 7–12

51. Li Z, Wang C, Lei T, Ma H, Su J, Ling S, Wang W (2019) Arched bamboo charcoal as interfacial solar steam generation integrative device with enhanced water purification capacity. Adv Sustain Syst 3:1800144
52. Chen Y, Sha C, Wang W, Yang F (2020) Solar-driven steam generation on nitrogen-doped graphene in a 2D water path isolation system. Mater Res Express 7:015507
53. Oginni O, Singh K, Oporto G, Dawson-Andoh B, McDonald L, Sabolsky E (2019) Influence of one-step and two-step KOH activation on activated carbon characteristics. Bioresource Technol Rep 7:100266
54. Shan X, Lin Y, Zhao A, Di Y, Hu Y, Guo Y, Gan Z (2019) Porous reduced graphene oxide/nickel foam for highly efficient solar steam generation. Nanotechnology 30:425403
55. Wang Y, Wang C, Song X, Megarajan SK, Jiang H (2018) A facile nanocomposite strategy to fabricate a rGO–MWCNT photothermal layer for efficient water evaporation. J Mater Chem A 6:963–971
56. Ghasemi H, Ni G, Marconnet AM, Loomis J, Yerci S, Miljkovic N, Chen G (2014) Solar steam generation by heat localization. Nat Commun 5:4449
57. Franciski MA, Peres EC, Godinho M, Perondi D, Foletto EL, Collazzo GC, Dotto GL (2018) Development of CO2 activated biochar from solid wastes of a beer industry and its application for methylene blue adsorption. Waste Manag 78:630–638
58. Zhang Y, Cheng Q, Wang D, Xia D, Zheng X, Li Z, Hwang J-Y (2019) Preparation of Pyrolytic carbon from waste tires for methylene blue adsorption. JOM-US 71:3658–3666
59. Wang Y, Zhang Y, Li S, Zhong W, Wei W (2018) Enhanced methylene blue adsorption onto activated reed-derived biochar by tannic acid. J Mol Liq 268:658–666
60. Tsai W-T, Bai Y-C, Lin Y-Q, Lai Y-C, Tsai C-H (2019) Porous and adsorption properties of activated carbon prepared from cocoa pod husk by chemical activation. Biomass Conv Bioref 10:35–43
61. Huang W, Chen J, Zhang J (2018) Adsorption characteristics of methylene blue by biochar prepared using sheep, rabbit and pig manure. Environ Sci Pollut R 25:29256–29266
62. Kueasook R, Rattanachueskul N, Chanlek N, Dechtrirat D, Watcharin W, Amornpitoksuk P, Chuenchom L (2020) Green and facile synthesis of hierarchically porous carbon monoliths via surface self-assembly on sugarcane bagasse scaffold: influence of mesoporosity on efficiency of dye adsorption. Microporous Mesoporous Mater 296:110005
63. Fan S, Wang Y, Wang Z, Tang J, Tang J, Li X (2017) Removal of methylene blue from aqueous solution by sewage sludge-derived biochar: adsorption kinetics, equilibrium, thermodynamics and mechanism. J Environ Cheml Eng 5:601–611
64. Tian D, Xu Z, Zhang D, Chen W, Cai J, Deng H, Sun Z, Zhou Y (2019) Micro–mesoporous carbon from cotton waste activated by $FeCl_3/ZnCl_2$: preparation, optimization, characterization and adsorption of methylene blue and eriochrome black T. J Solid State Chem 269:580–587
65. Mahdi Z, Hanandeh AE, Yu Q (2016) Influence of pyrolysis conditions on surface characteristics and methylene blue adsorption of biochar derived from date seed biomass. Waste and Biomass Valori 8:2061–2073
66. Li Z, Jia Z, Ni T, Li S (2017) Adsorption of methylene blue on natural cotton based flexible carbon fiber aerogels activated by novel air-limited carbonization method. J Mol Liq 242:747–756
67. Liu F, Chung S, Oh G, Seo TS (2012) Three-dimensional graphene oxide nanostructure for fast and efficient water-soluble dye removal. ACS Appl Mater Interfaces 4:922–927